Materials & Design 266 (2026) 116141

Contents lists available at ScienceDirect

Materials & Design

journal homepage: www.elsevier.com/locate/matdes

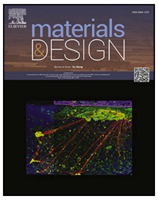

Temperature-dependent deformation mechanisms influenced by the μ phase TCP in a Ni-based single crystal superalloy

Sangwon Lee[a,b,c], Jeonghyeon Do[b], Baig Gyu Choi[b], Joong Eun Jung[b], In Soo Kim[b], Ujjval Bansal[c], Christoph Kirchlechner[c], Pyuck-Pa Choi[a,*], Subin Lee[c,*]

[a] *Department of Materials Science and Engineering, Korea Advanced Institute of Science and Technology (KAIST), Daejeon 34141, the Republic of Korea*
[b] *Aerospace Materials Research Center, Korea Institute of Materials Science (KIMS), Changwon 51508, the Republic of Korea*
[c] *Institute for Applied Materials, Karlsruhe Institute of Technology, Karlsruhe 76131, Germany*

ARTICLE INFO

Keywords:
Ni-based single crystal superalloy
Topologically close-packed (TCP) phase
Deformation behavior
Micropillar compression
High temperature

ABSTRACT

The influence of the plate-like μ phases precipitates in Ni-based single-crystal superalloys on their mechanical properties and deformation mechanisms was systematically investigated over a range of temperatures (25–700 °C) using multi-scale mechanical testing together with electron microscopy-based microstructure analysis. Macro-scale compression tests provided insights into the bulk mechanical performance, whereas *in situ* scanning electron microscope (SEM) micropillar tests enabled direct comparison of local deformation behaviors between μ phase-containing and μ phase-free regions. The results demonstrated that at room temperature, the μ phase remained undeformed and acted as an effective barrier to $\{111\}_{\gamma/\gamma'}$ slip propagation. However, at elevated temperatures ($\geq$ 500 °C), the μ phase exhibited distinct deformation modes, including bending and shearing along non-basal planes. In contrast to the temperature-dependent deformation behavior, the critical resolved shear stress (CRSS) of micropillars consistently decreased in the presence of μ phases, irrespective of temperature. This indicates that the observed CRSS reduction likely originated from microstructural changes in the surrounding γ/γ' rather than from deformation of the μ phase itself. This work clearly demonstrates temperature-dependent deformation behavior of the μ phase formed in Ni-based single-crystal superalloys and provides insights into a guidance for microstructural control and enhanced material reliability in high-temperature applications.

1. Introduction

Nickel-based single-crystal (SX) superalloys are widely used as structural materials in turbine blade components of aircraft engines and power-generation gas turbines, owing to their exceptional mechanical properties at temperature approaching 1700 °C at turbine inlet conditions [1,2]. To further enhance the thermal efficiency and overall performance of gas turbines, operation at higher temperature is essential [1–6]. However, prolonged exposure of Ni-based superalloys at temperatures exceeding 1000 °C inevitably results in the precipitation of topologically close-packed (TCP) phases, which have been widely reported to degrade mechanical properties [7–10].

To mitigate TCP phase formation, fourth-generation Ni-based SX superalloys commonly incorporate substantial amounts of Ru in the range of 3–6 wt%. Although Ru additions are effective in suppressing the formation of TCP phases, their use significantly increases overall material costs. For example, in some alloys, the combined cost of Re and Ru can account for more than 50% of the total alloy cost, despite their contents being only a few weight percent [11,12]. This economic drawback represents a major limitation to the widespread application of fourth- and higher-generation alloys. Furthermore, Ru addition is not universally beneficial; indeed, in certain alloy systems, Ru has been reported to promote TCP phase formation rather than suppress it [13–16]. Therefore, instead of relying solely on the addition of costly refractory elements to inhibit TCP phase formation, it is crucial to firstly develop a thorough understanding of TCP phase behavior under various conditions, which will clarify which aspects of the microstructure must be modified or controlled, thereby enabling more effective and economically viable alloy design strategies.

The detrimental impact of TCP phases on mechanical properties has frequently been attributed to their intrinsic brittleness and the susceptibility of their interfaces with the surrounding γ/γ' to crack initiation

---

* Corresponding authors.
E-mail addresses: p.choi@kaist.ac.kr (P.-P. Choi), subin.lee@kit.edu (S. Lee).

https://doi.org/10.1016/j.matdes.2026.116141
Received 19 January 2026; Received in revised form 5 April 2026; Accepted 27 April 2026

and propagation [7–10]. However, most previous studies have relied on *postmortem* analyses of crack distributions in fractured specimens [17–23], providing limited insight into the specific role of TCP phases during deformation and interaction with other defects, for example dislocations. Moreover, TCP phases exhibit substantial variation in crystal structure and morphology—including μ, σ, P, and R phases with various shapes such as plate-like, needle-like, and spherical—further complicating generalized interpretations. In addition, several studies have challenged the conventional view that TCP phases inevitably degrade mechanical properties [17,24]. Micromechanical tests, such as nanoindentation and micropillar compression on C14 Laves phases and μ phases, have revealed plasticity via activation of basal and non-basal slip systems [25–31], contradicting the long-standing expectation of purely brittle behavior in intermetallic compounds. These findings suggest that TCP phases should not be regarded simply as crack initiation sites. Instead, their influence on alloy deformation is dependent on their crystal structure, morphology, and crystallographic orientation within the γ/γ' microstructure of superalloys. Consequently, a thorough understanding of the deformation behavior of each TCP phase type is essential for assessing their influence on the mechanical performance of Ni-based superalloys and for integrating this knowledge into alloy design strategies.

In our previous study, the deformation behavior and mechanical properties associated with plate-like μ-type TCP phases were investigated at room temperature using *in situ* micropillar compression tests [32]. The μ phase was found to strongly suppress slip activity on planes not parallel to TCP plates, confining deformation primarily to {111} planes aligned parallel to the TCP plates. Notably, deformation did not occur directly at the μ/γ' interfaces – regions expected to be mechanically vulnerable – but rather at locations a few tens of nanometers away, a phenomenon attributed to local order strengthening induced by Ta diffusion near the interface.

Following these findings, the present study aims to further elucidate the influence of plate-like μ phases on deformation behavior and mechanical properties at elevated temperatures up to 700 °C. Macro-scale compression tests were conducted to quantify the overall effect of μ phase formation on the alloy, while *in situ* scanning electron microscope (SEM) micropillar compression tests were conducted to directly investigate the local deformation mechanisms associated with individual μ phases. The results provide deeper insights into how μ phases affect the mechanical performance of Ni-based superalloys as a function of temperature, clarifying the underlying deformation mechanisms operative within the μ phases. Ultimately, this work contributes toward a more comprehensive understanding of μ phases, thus informing future alloy design strategies and enhancing material reliability under extreme operating conditions.

2. Experimental procedure

This study employs a single-crystal Ni-based superalloy which consists of 14.8 wt% of (Al + Ti + Ta) and 27.6 wt% of (Co + Cr + Mo + W) balanced with Ni. The alloy was produced using directional solidification via the Bridgman vacuum induction melting technique in a cylindrical shape with a length of 160 mm and a diameter of 13 mm. After casting, the material underwent a solution treatment at 1300 °C for 1 h under an Ar atmosphere, followed by a two-step aging process (1140 °C for 2 h and 871 °C for 20 h) to establish the γ/γ' microstructure. Two samples were used in this study; the first one is as-aged specimen which will be referred to as “unexposed” in the rest of the manuscript. The other one is “exposed” sample with a high density of μ phases. To promote μ phase formation, the aged specimen was then subjected to thermal exposure at 1000 °C for 30 min.

For the metallography, the samples were mechanically ground with SiC paper and polished with diamond suspensions and OP-S. The polished samples were etched with Kalling’s reagent ($CuCl_2$ + HCl + ethanol). The microstructure was observed by a field emission scanning electron microscopy (FE-SEM, JSM-7001F, Jeol). The compositions of the γ' and μ phases were characterized by atom probe tomography (APT, LEAP 4000X HR, Cameca) with a detection rate of 0.5%, a laser energy of 60 pJ, a pulse frequency of 125 kHz, and a base temperature of 50 K. The APT tip was prepared by a focused ion beam (FIB, Helios G4, Thermo Fisher Scientific). The 3D reconstruction was conducted by using AP Suite 6.3 (Cameca).

Multi-scale compression testing was selected to enable stable plastic deformation at the onset of yielding without premature fracture, thereby allowing direct evaluation of critical resolved shear stress (CRSS) and subsequent microstructural characterization. Since the primary objective of this study is to investigate slip–μ interactions at yield-level strains, compression provides a controlled framework to isolate crystallographic deformation mechanisms. In this regime, the fundamental dislocation processes are not expected to be significantly affected by the loading mode, whereas differences between tension and compression become more pronounced at higher strains where fracture and damage evolution dominate. To measure the macro-scale mechanical properties, cylindrical specimens with a diameter of 3 mm and a height of 6 mm were prepared. The compression tests were conducted at temperatures of 25, 500, and 700 °C with a displacement rate of 0.36 mm/min by using a high temperature property testing machine (Landmark Servo-hydraulic Test System, MTS). After compression tests, electron channeling contrast imaging (ECCI) was employed to observe the defect structures of the plastically 3% compressed specimens by using FE-SEM (Merlin, Zeiss) with a voltage of 20 kV, a working distance of 6 mm, and a probe current of 20 nA. Additionally, crystallographic analysis was conducted from conventional transmission electron microscopy (TEM) imaging, as well as high-angle annular dark field (HAADF)-scanning transmission electron micrographs (STEM) acquired from FE-TEM (JEM-F200, Jeol) and double C_S-corrected FE-TEM (Titan cubed G2, Thermo Fisher Scientific).

To evaluate the micro-scale mechanical properties, micropillar specimens with a diameter of 1 μm and a height of 2 μm were prepared by a FIB workstation (Crossbeam 550 L, Zeiss). For the milling process, Ga^+ ions at 30 keV were utilized, with the current set of 30 nA for rough milling, 3 nA for intermediate milling, and 0.7 nA for final milling. The taper angle was kept below 3°. The μ-free specimens were fabricated from the unexposed sample, while the μ-containing specimens were fabricated from the exposed sample. The micropillar compression tests were conducted in a FE-SEM (Merlin, Zeiss) equipped with an *in situ* SEM indenter (Hysitron PI-89, Bruker) in a displacement-controlled mode at temperatures of 25, 500, and 700 °C. For the indenter tips, a diamond flat punch with diameter of 2 μm (Synton MDP) and a WC flat punch with diameter of 5 μm (Synton MDP) were used at room temperature and high temperature, respectively.

3. Results

3.1. Formation of μ phases during high-temperature exposure

Fig. 1 presents the microstructural evolution of single-crystal Ni-based superalloy during high-temperature exposure, observed along the $[001]_{\gamma/\gamma'}$ direction, which corresponds to the loading direction in compression tests. As shown in Fig. 1a and d, μ phases were identified within the microstructures located in dendrite core regions both the unexposed and exposed samples. Even in the unexposed sample, which was subjected only to the standard solution and aging processes, the formation of μ phases was confirmed (Fig. 1a). Their precipitation is attributed to the relatively high content (27.6 wt%) of TCP-forming elements (Cr, Co, Mo, and W) in the present alloy system. These elements are known to segregate preferentially into dendrite core regions during solidification, thereby locally enriched conditions favorable for μ phase formation [13,19]. Following the additional high-temperature exposure, the exposed sample exhibited a significantly increased population of μ

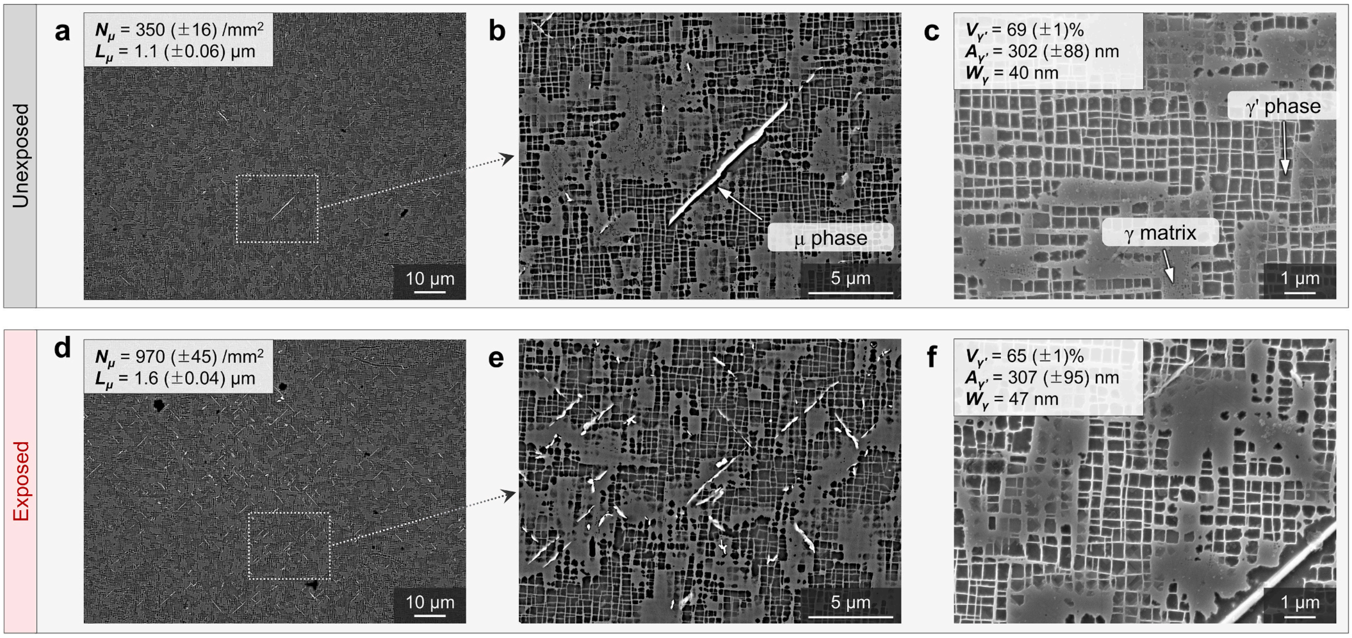

Fig. 1. SEM micrographs acquired along $[001]_{\gamma/\gamma'}$ direction of the (a–c) unexposed and (d–f) exposed single-crystal specimens: (a, d) The distribution of μ-type TCP phases in dendrite core regions, where N_μ and L_μ denote the number density and average length of μ phases, respectively, (b, e) magnified images of the microstructure containing μ phases, and (c, f) microstructures of γ/γ' in dendrite core regions, where $V_{\gamma'}$, $A_{\gamma'}$, and W_γ denote the volume fraction of γ', average size of γ', and γ channel width, respectively.

phases compared to the unexposed condition, indicating that thermal exposure further promotes μ phase precipitation (Fig. 1d). The magnified images in Fig. 1b and e reveal a characteristic γ/γ'/μ microstructure, comprising γ matrix, cuboidal-shaped γ' phase, and plate-like μ phase aligned along $\{111\}_{\gamma/\gamma'}$. Quantitative analysis of μ phase number density (N_μ) in Fig. 1a and d indicates a significant increase after thermal exposure. While the number density of μ phase was measured to be 350 ± 16 per mm^2 in the unexposed sample, it increased approximately 3 times in the exposed sample, reaching 970 ± 45 per mm^2, where errors denote the standard deviations of the measured values from three images for each sample. Additionally, the average length (L_μ) slightly increased from 1.10 ± 0.06 μm (unexposed) to 1.60 ± 0.04 μm (exposed) where errors represent standard deviations. Measurements of length and number density of the μ phase were carried out over identical analyzed areas of 15,036 μm^2 for each sample, yielding total number of μ particles of 522 (unexposed) and 1,452 (exposed).

The microstructural characteristics of γ/γ' before and after high-temperature exposure are shown in Fig. 1c and f, respectively. It was observed that there was no significant change in the cuboidal morphology of γ' precipitate during exposure process. The volume fraction of γ' precipitates ($V_{\gamma'}$), determined by lever rule from APT compositional data obtained from same specimens [32], slightly decreased from 69 (±1)% for unexposed sample to 65 (±1)% for exposed sample. In contrast, the average size of γ' precipitates ($A_{\gamma'}$) increased from 302 (±88) nm to 307 (±95) nm during exposure process. Under the assumption that the γ' precipitates are perfectly cubic, the width of γ channel (W_γ) can be calculated from the γ' volume fraction ($V_{\gamma'}$) and the average γ' precipitate size ($A_{\gamma'}$) using the following equations:

$$V_{\gamma'} = \frac{{A_{\gamma'}}^3}{(A_{\gamma'} + W_\gamma)^3} \tag{1.1}$$

$$W_\gamma = A_{\gamma'}\left({V_{\gamma'}}^{-1/3} - 1\right) \tag{1.2}$$

Using these equations, the width of γ channel was determined to increase from 40 nm in the unexposed to 47 nm in the exposed. This widening of the γ channel is attributed primarily to the reduction of γ' volume fraction after exposure process.

The crystallographic information of the μ and its surrounding γ' phases is depicted in Fig. 2. The crystal structure of γ' phase is $L1_2$ structure with lattice parameter of $a = 0.36$ nm, and μ phase has rhombohedral lattice system (space group $R\bar{3}m$, Co_7Mo_6 prototype) with lattice parameters of $a = 0.48$ nm and $c = 2.59$ nm, which were measured from high-resolution TEM image in our previous study [32]. As observed in the high-resolution TEM image in Fig. 2b, the γ'/μ interface is flat, and the orientation relationship of the γ'/μ interface is determined to be $[\bar{2}1\bar{1}]_{\gamma'}\|[11\bar{2}0]_\mu$ and $\{111\}_{\gamma'}\|(0001)_\mu$. Also, the interface exhibits a semi-coherent nature with a misfit strain of 7.5% [32], which contributes to the formation of plate-like morphology by minimizing the total interfacial energy through broadening along low-energy interface plane [24,33].

To quantify the chemical composition of the μ phase, APT analysis was conducted, which offers the spatial and compositional resolution for the nanoscale (about 200 nm thickness) and multicomponent (containing 8 alloying elements) μ phase. As represented in Fig. 2c, a site-specific lift-out was conducted by FIB from the region with the μ phase surrounded by γ', followed by annular milling into needle-shaped tip for APT analysis. A composition profile was obtained using proximity histogram analysis across the γ'/μ interface. The proximity histogram reveals clear partitioning of refractory solutes into μ phase: >30% W, >20% Cr, ~19% Ni, ~16% Co, and ~5% of Mo (at.%), while γ'-forming elements Al, Ti, and Ta are nearly absent within the μ phase. This composition result rationalizes the microstructural observation in Fig. 1 that the μ phase preferentially precipitates in dendrite cores, where segregation of W, Cr, and Mo provides the local solute supply for μ phase formation. Further crystallographic and chemical compositional details are available in our previous work [32], which analyzed the same material and specimen batch used in the present study.

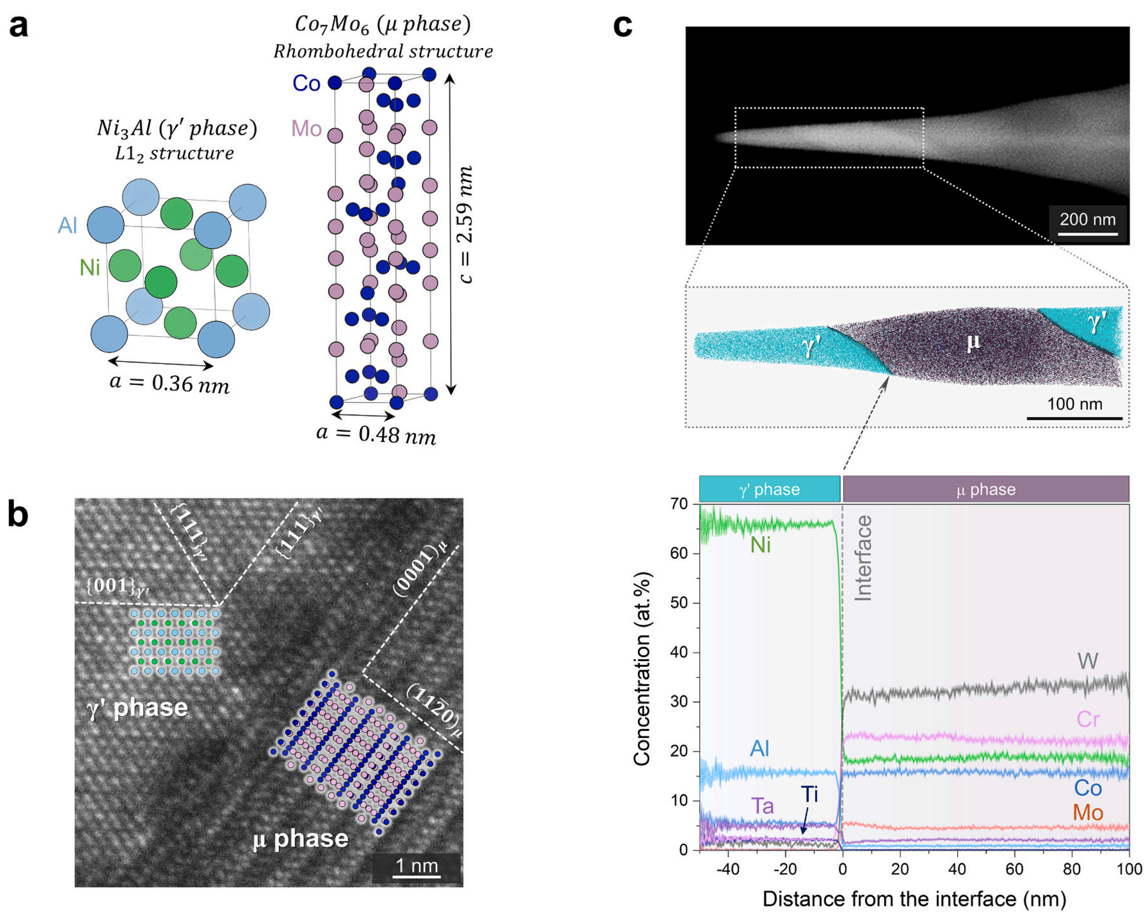

Fig. 2. (a) The crystal structures of the γ' and μ phases (prototype Co_7Mo_6), (b) an atomic-resolution TEM image representing the interface nature of those phases. The crystallographic orientations and lattice parameters were obtained from the high-resolution TEM image and selected-area electron diffraction (SAED) in our previous report [32]. (c) A SEM image and 3D atom map of a μ-containing APT specimen, and a proximity histogram displaying elemental distribution near the γ'/μ interface obtained from APT.

3.2. Temperature dependency of the mechanical property: Macro-scale compression

To examine the influence of μ phases on mechanical property, the macro-scale compression tests were conducted at various temperatures as representative resulting stress–strain curves are shown in Fig. 3. The diameter of specimen is 3 mm, which contains approximately 70 dendrites, such that the measured response represents the overall bulk behavior of the alloy and excludes the influence of local elemental segregation between dendrite core and interdendritic regions. Given the limited number of specimens, the unexposed sample was tested at 25, 500, and 700 °C, whereas the exposed sample was tested at 25, 500, 600, 700, 800, 900 °C in order to establish the onset temperature of the yield anomaly – an increase in yield strength with increasing temperature – in this alloy system. In the case of the unexposed sample (Fig. 3a), which contains fewer μ phases, the stress–strain curve exhibited the highest yield strength of 1167 ± 5 MPa at 25 °C. As the testing temperature increased to 500 °C, the yield strength decreased to 1085 ± 28 MPa and remained nearly constant at 1094 ± 26 MPa at 700 °C. Errors denote the standard deviations of the measured values from two results for each

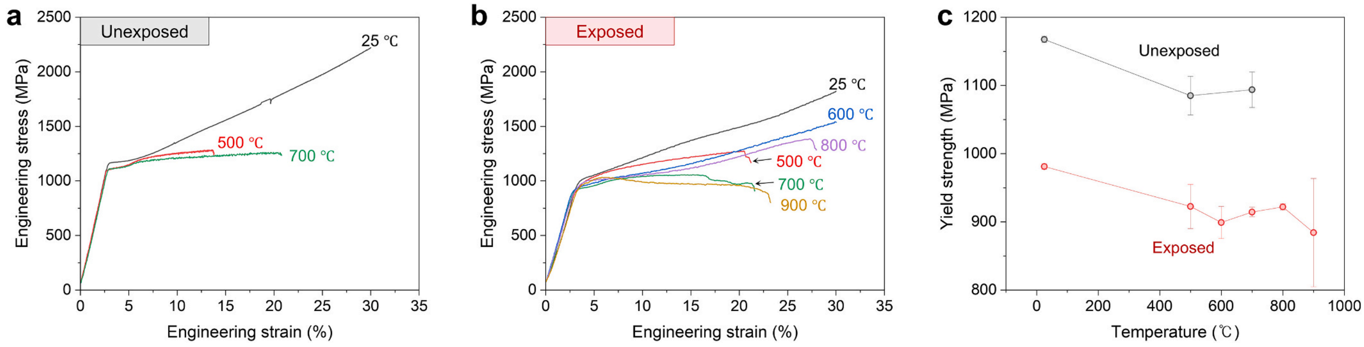

Fig. 3. Macro-scale compression engineering stress–strain curves obtained from cylindrical specimens with 3 mm diameter for the (a) unexposed tested at 25–700 °C and (b) exposed samples tested at 25–900 °C. (c) Temperature dependence of yield strength of unexposed and exposed samples, where error bars denote standard deviations of measured values from two results for each condition. The compression tests were conducted along the $[001]_{\gamma/\gamma'}$ direction.

condition.

In the case of the exposed sample (Fig. 3b), which contains a higher density of μ phases, yield strength was reduced to 981 ± 4 MPa at 25 °C compared to that of the unexposed sample. This yield strength further decreased to 899 ± 24 MPa at 600 °C, followed by a mild increase up to 800 °C, and then a sharp drop at 900 °C, indicating the onset of yield anomaly phenomenon around 700–800 °C for this alloy (Fig. 3c). Therefore, although 700 °C does not correspond to the peak of the yield anomaly, it appears to lie within the plateau transition range where the strengthening effect partially recovers. This is particularly evident in the unexposed sample, where the yield strength at 700 °C slightly exceeds that at 500 °C, suggesting the presence of a weak yield anomaly. Since the primary focus of this study is to investigate the influence of μ phase at temperature below the peak, our interpretation of the mechanical properties and microstructure in the following section is limited to 700 °C. This choice was further motivated by comparison with *in situ* SEM micropillar experiments in the following section, where the high surface-to-volume ratio can promote high-temperature deformation mechanisms at slightly lower temperatures.

Across the entire temperature range, the yield strength of the exposed sample with a higher density of μ was consistently and significantly lower than that of the unexposed sample (Fig. 3c). The differences in the average yield strength between those two samples were 186 MPa at 25 °C, 162 MPa at 500 °C, and 179 MPa at 700 °C, respectively.

3.3. *Deformed microstructure analysis*

Detailed deformation mechanisms were investigated by *postmortem* microstructure analysis using ECCI and TEM. Firstly, Fig. 4 presents the deformed microstructure near μ phase in the sample compressed to 3% plastic strain at 25 °C. The cross-sectional sample was observed from $[100]_{\gamma/\gamma'}$ orientation to clearly resolve the dislocation structures and their interactions with the μ phases. In the representative ECCIs in Fig. 4a–c, dislocations appear as bright lines and predominantly glide along the $\{111\}_{\gamma/\gamma'}$ slip planes, consistent with the primary slip system in FCC superalloys. Please note that microstructure analysis in this section was conducted on the deformed unexposed specimen. Although the volume fraction of μ phases is relatively low in the unexposed sample, their fundamental deformation behavior is expected to be the same regardless of precipitate density. Therefore, detailed ECCI/TEM analysis was carried out on the unexposed specimen, as isolated μ phases provide a clearer view of dislocation–μ phase interactions.

Notably, upon approaching the μ phases, the dislocations were found to be disrupted or blocked at the μ/γ' interface, indicating an obstruction to slip transmission across the interface. This behavior was consistently observed through all μ-containing regions (Fig. 4a–c), suggesting that the μ phase serves as a strong barrier to dislocation motion along the $\{111\}_{\gamma/\gamma'}$ slip planes at room temperature. A magnified image of Region III near the μ phase is shown in Fig. 4d. In the backscattered electron (BSE) image, dislocations are seen to accumulate at the μ/γ' interface, appearing as intense contrast lines. Simultaneously, the secondary electron (SE) image of the same region reveals no evidence of plastic deformation within the μ phase itself under the applied compressive stress. These observations clearly demonstrate that at 25 °C, the μ phase remains mechanically undeformed, and acts as an effective obstacle to dislocation motion. As a result, dislocations either alter their propagation paths to bypass the μ phases or activate secondary dislocation source through the stress field generated by pile-ups so that slip can continue across the μ phases. This behavior is distinctly shown in Regions I and II of Fig. 4a and b, respectively, where dislocation structures clearly circumvent the μ phases rather than penetrating or deforming them.

In contrast to the room temperature deformation, dislocation blocking by the μ phase was barely observed at 700 °C (Fig. 5). As shown in the magnified BSE image from Region I in Fig. 5b, dislocations cut through the μ phase. The corresponding SE image shows shearing of the precipitate as well as bending suggesting that the μ phase underwent plastic deformation or even fracture. Similar behavior is observed in Region II (Fig. 5c and d). Dislocations on the $\{111\}_{\gamma/\gamma'}$ slip planes appear to fracture the μ phase into several fragments and continue gliding beyond the phase boundary. The corresponding SE image provides further evidence, showing multiple shearing traces along the $\{111\}_{\gamma/\gamma'}$ slip planes, confirming that the μ phase has undergone severe fracture. Furthermore, as indicated by the white dashed lines in Fig. 5d, offsets between the slip traces before and after crossing the precipitate show that $\{111\}_{\gamma/\gamma'}$ slip does not simply pass through the μ phase, but instead

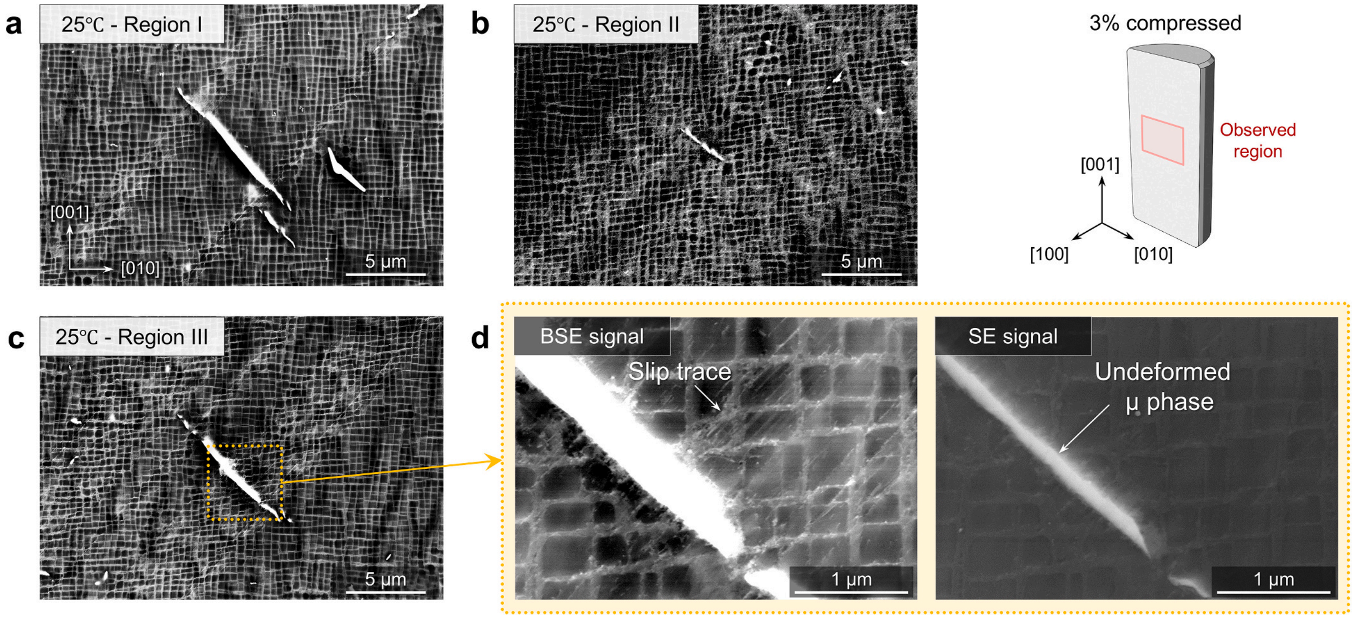

Fig. 4. ECCIs obtained from the longitudinal mid-section of the unexposed specimen plastically 3% compressed at 25 °C along the $[001]_{\gamma/\gamma'}$ direction, observed from the $[100]_{\gamma/\gamma'}$ direction. (a–c) Representative images from different regions showing the dislocation structures around μ phases. (d) Magnified images of Region III from (c), representing detailed dislocation arrangements near the μ phase using BSE signal, and the morphology of the μ phase using SE signal after deformation.

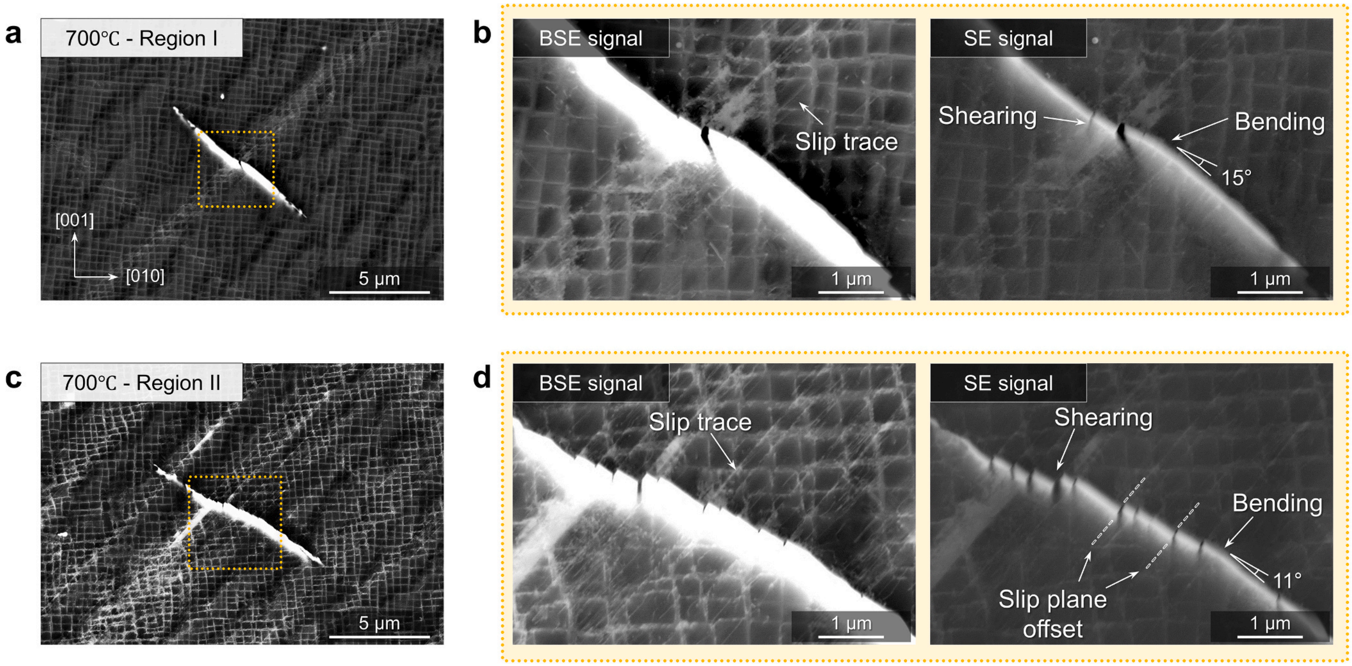

Fig. 5. ECCIs obtained from the longitudinal mid-section of the unexposed specimen plastically 3% compressed at 700 °C along the $[001]_{\gamma/\gamma'}$ direction, observed from the $[100]_{\gamma/\gamma'}$ direction. (a, c) Representative images from two distinct regions showing deformation of μ phases at elevated temperature. (b, d) Magnified images of Region I from (a) and Region II from (c), respectively, representing detailed dislocation arrangements near the μ phase using BSE signal, and the bending and shearing of the μ phases using SE signal after deformation. White-colored dashed lines in (d) indicate $\{111\}_{\gamma/\gamma'}$ slip plane transition after shearing μ phase.

follows a cross-slip-like process; it first changes its path onto specific slip planes within the μ phase and then returns to the $\{111\}_{\gamma/\gamma'}$ slip plane to continue gliding in the γ/γ' matrix. This interpretation is further supported by the observation that the fractured planes form at specific orientation, indicating that they are not randomly formed but result from dislocation glide on certain crystallographic planes. A more detailed discussion of this mechanism is provided in Section 4.1. In summary, the μ phase exhibits a clear temperature-dependent transition in its mechanical behavior and its role in the deformation mechanisms. While the μ phase remains rigid and acts as dislocation barriers at room temperature, at elevated temperatures it loses this resistance, undergoes plastic deformation or brittle shear fracture, thereby allows slip transmission through μ phase regions. This behavior is consistently observed in both unexposed and exposed conditions (Supplementary Fig. S3).

To get deeper insight into the deformation behavior of μ phases during macro-scale compression, detailed (S)TEM analysis was performed on a region containing the μ phase in the unexposed specimen compressed plastically to 3% strain along the $[001]_{\gamma/\gamma'}$ direction at 700 °C. As shown in Fig. 6a, TEM observation along the $[110]_{\gamma/\gamma'}$ clearly reveals that the plate-like μ phase is aligned parallel to the $(\bar{1}11)_{\gamma/\gamma'}$ evidenced by the sharp interfaces in edge-on imaging condition, while distinct slip traces within the γ/γ' matrix predominantly appear along the $(1\bar{1}1)_{\gamma/\gamma'}$. A SAED acquired from Region A shows the crystallographic orientations of γ/γ' and μ phases (see Fig. 6b). Previous studies reported that $[0001]_\mu$ direction is parallel to $\langle 111\rangle_{\gamma/\gamma'}$ in the undeformed initial microstructure [7,24,32,34]. However, the present SAED exhibits an 8° rotation of $[0001]_\mu$ as evidenced by the presence of faint spots of $(0003n)_\mu$, where n is integer, parallel to $(\bar{1}11)_{\gamma/\gamma'}$ together with slightly rotated $(0003n)_\mu$ diffraction spots. This observation implies the coexistence of undeformed and distorted regions within the μ phase, indicating that deformation-induced bending of the μ phase can occur.

Magnified images of Region A (Fig. 6c and d) clearly show deformation-induced defects inside the μ phase, demonstrating that both the prismatic $(11\bar{2}0)_\mu$ plane (highlighted in red) and the pyramidal slip plane (highlighted in blue) with an inclination angle of approximately 65° with respect to the basal plane. In addition, the slip trace in the γ/γ' matrix appears continuously with those in the μ phase, providing evidence that dislocations are transmitted across the interface and continue to glide. Complementary observations from Region B (Fig. 6e and f) and other TEM specimens (Fig. 6i and j) provide additional insights into the deformation pathway. Specifically, the STEM-HAADF images of Region B (Fig. 6e) and the other specimen (Fig. 6i and j) shows $\{111\}_{\gamma/\gamma'}$ slip traces within the γ/γ' matrix interacting with the μ phase and subsequently propagating along adjacent $\{111\}_{\gamma/\gamma'}$ planes separated by a few atomic layers from initial slip plane, suggesting the occurrence of slip plane transition after shearing μ phase. This clearly indicates that the slip does not simply shear through the μ phase, but rather it transfers onto particular slip planes of the μ phase in a manner of cross-slip-like behavior. Additionally, a high magnification HAADF image in Fig. 6f reveals activation of a pyramidal slip with an inclination angle of 61° and defects on basal plane, suggesting that a limited amount of basal slip was also operative. In the case of Region C (Fig. 6g and h), clear atomic steps indicative of both $< c >$ or $< c + a >$ prismatic and pyramidal slip mechanisms are observed. The measured inclination angle for the pyramidal slip plane is approximately 69°, confirming the presence of multiple pyramidal slip systems within the μ phase.

3.4. *Dislocation–μ phase interactions revealed by micropillar compression*

While macro-scale experiments provided insights into the overall mechanical properties influenced by μ phases at various temperatures, along with *postmortem* analyses revealing internal deformation mechanisms, a more detailed understanding requires examining the behavior of individual precipitates. In this section, *in situ* SEM high-temperature micromechanical tests were conducted on the pillars with μ-free and μ-containing, which are designed to contain a single μ phase within the specimen. By isolating individual precipitates, these tests allow direct evaluation of their contribution to the local mechanical properties and enable a closer examination of the underlying deformation mechanisms through slip-trace analysis at different temperatures. The micropillar

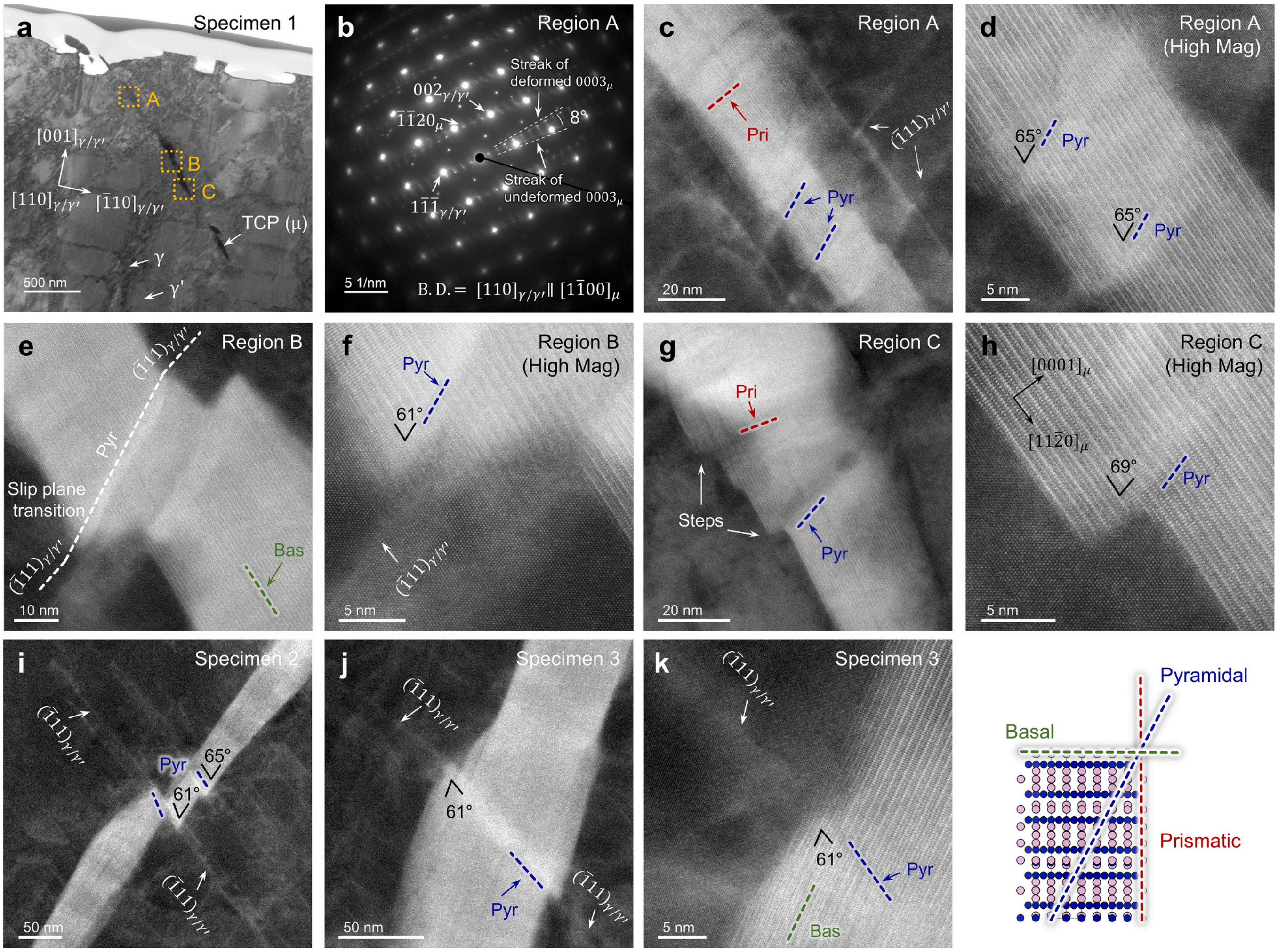

Fig. 6. TEM and STEM results of the unexposed sample compressed by 3% along the $[001]_{\gamma/\gamma'}$ direction at 700 °C. (a) Overview TEM bright field (BF) image of the lamella specimen observed from the $[110]_{\gamma/\gamma'}$ direction, showing the distribution of γ, γ', and μ phases. (b) SAED obtained from Region A, revealing the crystallographic orientations of γ/γ' and μ phases, and an 8° rotation of $[0001]_{\mu}$ induced by deformation. (c–k) STEM high-angle annular dark field (HAADF) images from (c, d) Region A, (e, f) Region B, (g, h) Region C, and (i–k) other TEM specimen, respectively, showing shear deformation along basal (Bas), prismatic (Pri) and pyramidal (Pyr) planes within the μ phase. An inset figure in the right bottom shows the crystallographic orientation of μ phase.

experiments were conducted up to 700 °C to maintain consistency with the dislocation-controlled deformation regime identified in the macroscopic tests, which exhibit a yield anomaly with peak strength at ~700–800 °C and a subsequent yield drop at higher temperatures, indicating a transition in deformation mechanism. In addition, to exclude potential influences arising from elemental segregation between dendrite core and interdendritic regions, all micropillars were fabricated exclusively from dendrite core regions where μ precipitation preferentially occurs and local chemistry is relatively consistent.

Stress–strain curves of each pillar deformed at different temperatures are shown in Fig. 7. Both samples, exposed and unexposed samples, showed similar behavior. Firstly, all curves exhibited well-defined yielding followed by load drops associated with discrete slip events. Unlike macro-scale compression results in Fig. 3, which represent softening behavior as temperature increases, no significant changes in the strain hardening were observed in the overall deformation behavior as the temperature increased from 25 to 700 °C. In the case of micropillar compression, the lateral stiffness as weak as the frictional stress between the tip and the sample may result in apparent strain hardening strongly dependent on the testing machine and protocol [35]. Consequently, we did not quantify the apparent strain hardening in this work. While the stress–strain curves of both specimens show similar trends, statistical analysis of the critical resolved shear stress (CRSS), determined from the 2% strain offset stress and Schmid factor for the activated slip system, revealed a decrease in the yield stress for the μ-containing pillars (Fig. 7h–j). The Schmid factors for the $\{111\}_{\gamma/\gamma'}$ slip system were 0.44 for unexposed specimens and 0.41 for exposed specimens, respectively, as determined in our previous study [32]. The cumulative distribution functions (CDFs) of CRSS at different temperatures, fitted with normal distribution functions, indicate that unexposed specimens consistently exhibit higher CRSS values. At 25 °C, the difference is approximately 50 MPa, whereas at 700 °C, the CRSS of the pillars without μ-phase precipitates is higher by about 130 MPa. The shaded bands around each fitted curve indicate the 95% confidence intervals. In addition, CRSS scatter increases with testing temperature. Although the number of tested pillars is inherently limited, the observed trends are consistent across repeated measurements and remain statistically distinguishable within the calculated confidence intervals. The lower CRSS values observed in the exposed specimens are counterintuitive, considering the presence of a hard precipitate phase, even in small volume fractions. It could be attributed to local chemical composition changes near the μ phase and the resulting microstructural changes: the decreased solid solution strengthening in the γ matrix and the reduced γ' volume fraction, as previously identified in our previous study [32].

Noteworthy is that, while the macro-scale compression results presented in Fig. 3 demonstrated a decrease in yield strength with

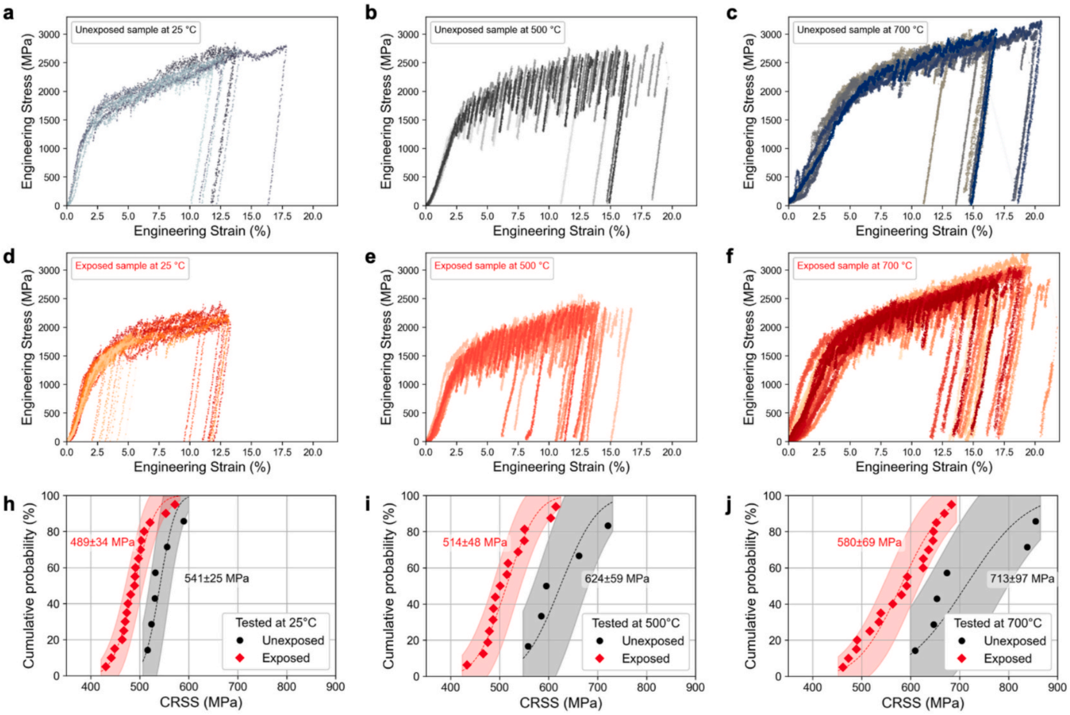

Fig. 7. Engineering stress–strain curves obtained from micromechanical tests performed on micropillars (1 μm diameter) fabricated from (a–c) unexposed (μ-free) and (d–f) exposed (μ-containing) specimens, and cumulative distribution functions (CDFs) of critical resolved shear stress (CRSS) at various temperatures: (a, d, h) 25 °C, (b, e, i) 500 °C, and (c, f, j) 700 °C. The grey and red-shaded bands indicate 95% confidence intervals for the unexposed (μ-free) and exposed (μ-containing) specimens, respectively. CRSS values were calculated using Schmid factors of 0.44 for the unexposed samples and 0.41 for the exposed samples, which were obtained from our previous report [32]. The number of tested micropillars for each condition was as follows: 25 °C (unexposed: n = 6, exposed: n = 19), 500 °C (unexposed: n = 5, exposed: n = 15), and 700 °C (unexposed: n = 19, exposed: n = 6). (For interpretation of the references to colour in this figure legend, the reader is referred to the web version of this article.)

increasing temperature for both samples, the micro-scale compression results in Fig. 7 exhibit the opposite trend, with CRSS increasing as temperature rises. Mean CRSS values for the μ-free specimen increased from 550 MPa at 25 °C to 624 MPa at 500 °C, and further to 713 MPa at 700 °C. For the μ-containing specimens, the corresponding values were 489, 514, and 580 MPa. The possible origin for the contrasting temperature dependencies between macro- and micro-scale tests will be discussed in Section 4.2.

To gain more mechanistic understanding, the deformed microstructure, specifically slip traces were analyzed using SEM imaging. The representative SEM images of the μ-free micropillar specimens fabricated from the unexposed sample before and after compression at 25, 500, and 700 °C. The loading direction was $[001]_{\gamma/\gamma'}$ and observation was made from $[100]_{\gamma/\gamma'}$ direction. Initially, all specimens consisted solely of γ/γ' phases. As shown in Fig. 8a, the deformed specimen at 25 °C exhibits multiple slip bands along $\{111\}_{\gamma/\gamma'}$ slip system. This behavior arises because multiple $\{111\}_{\gamma/\gamma'}$ slip systems have similar Schmid factors when compressed along $[001]_{\gamma/\gamma'}$ direction. A similar slip behavior was observed at 500 °C (Fig. 8b), with slip traces indicating activation of multiple $\{111\}_{\gamma/\gamma'}$ slip systems. Although surface oxidation at 700 °C makes clear identification challenging in Fig. 8c, faint slip traces can still be discerned, suggesting the same slip behavior was operative. These observations collectively indicate that multiple $\{111\}_{\gamma/\gamma'}$ slip behavior in μ-free regions remain consistent across the tested temperature range, regardless of temperature variation.

In the case of μ-containing specimens, their microstructure including μ phase was clearly visible before deformation (Fig. 9). At room temperature (Fig. 9a), examination of the μ phase morphology and surrounding slip traces before and after deformation indicates that the μ

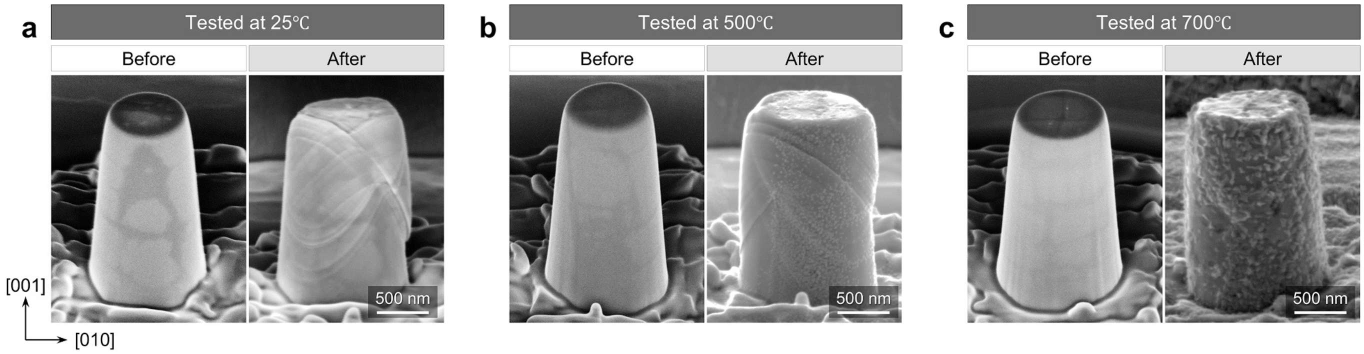

Fig. 8. Representative SEM images of micropillars (1 μm diameter) from the unexposed (μ-free) specimen, comparing slip behavior before and after micropillar compression testing conducted along the $[001]_{\gamma/\gamma'}$ direction at (a) 25 °C, (b) 500 °C, and (c) 700 °C.

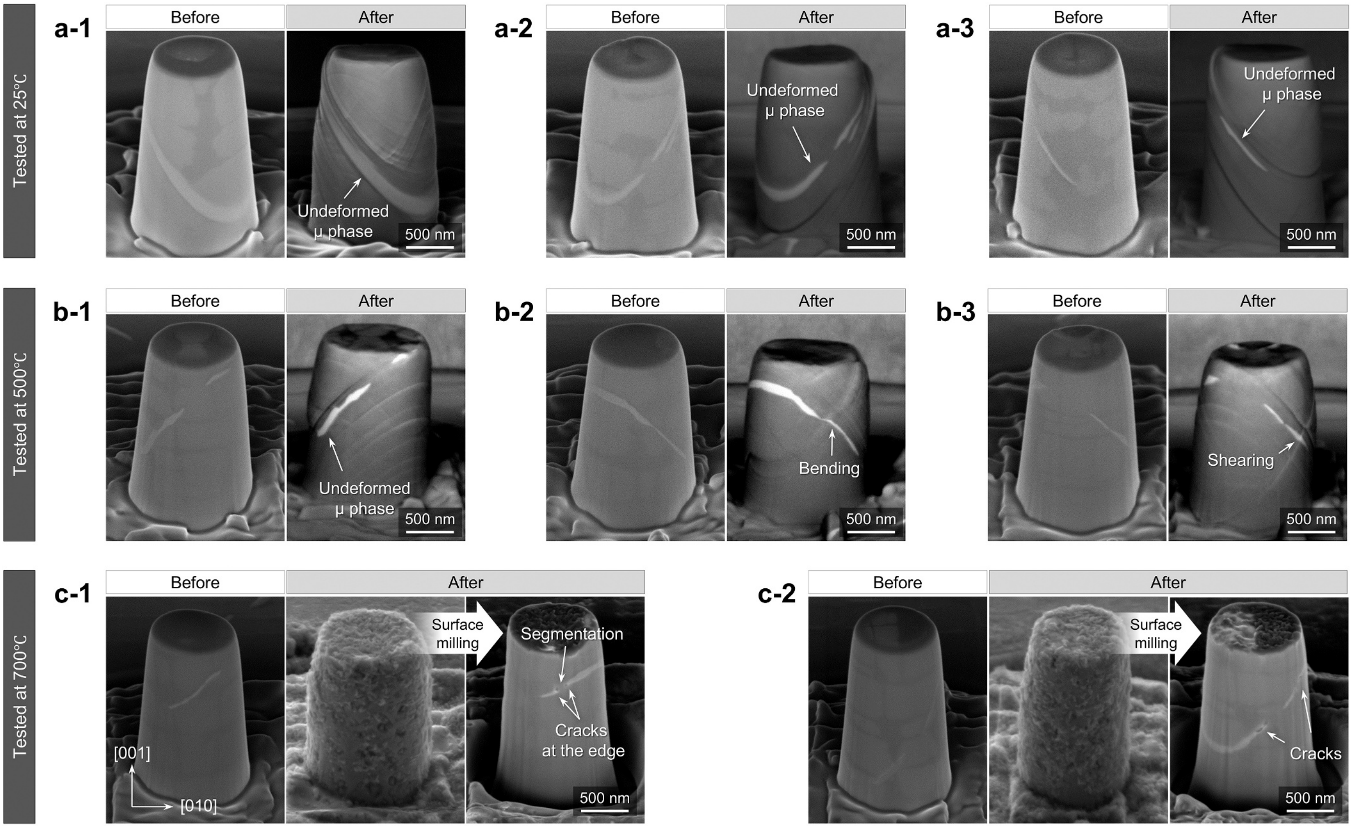

Fig. 9. Representative SEM images of micropillars (1 μm diameter) from the exposed (μ-containing) specimen, comparing their morphologies before and after micropillar compression testing conducted along the $[001]_{\gamma/\gamma'}$ direction at (a) 25 °C, (b) 500 °C, and (c) 700 °C. For the specimens tested at 700 °C, additional image after surface milling was represented to reveal the μ phase morphology from surface oxidation.

phase remained undeformed. Although multiple slip systems along the $\{111\}_{\gamma/\gamma'}$ planes were activated, slip primarily occurred on planes parallel to the μ phase. Non-parallel $\{111\}_{\gamma/\gamma'}$ slip systems appeared to be effectively blocked, consistent with the earlier ECCI results from macro-scale compression tests at 25 °C (see Fig. 4), reconfirming the role of μ phases as strong obstacles to slip at ambient conditions. However, at an intermediate temperature of 500 °C (Fig. 9b), additional deformation mechanisms were observed. In Fig. 9b-1, the μ phase remained intact, similar to the results at 25 °C, with slip predominantly occurring along planes parallel to the μ phase. Conversely, in another specimen in Fig. 9b-2, the non-parallel $\{111\}_{\gamma/\gamma'}$ slip system was activated cutting through the μ phase, inducing pronounced bending deformation of the μ phase, as evidenced by the morphological changes observed before and after compression. Furthermore, in Fig. 9b-3, slip was observed directly shearing through the μ phase, further demonstrating the variability in deformation mechanisms at elevated temperatures. At the highest test temperature of 700 °C (Fig. 9c), clear slip traces could not be directly identified due to severe surface oxidation. Therefore, additional FIB milling was conducted to remove the surface layer of the pillar and analyze internal deformation features after the deformation. Subsequent SEM observations of the milled surfaces revealed distinct internal defects in the μ phases. In Fig. 9c-1, distinct damage including segmented μ phases accompanied by visible cracks at the fracture edges was apparent. Similarly, Fig. 9c-2 exhibited cracks at the edges of the μ phases, highlighting their susceptibility to fracture at elevated temperatures.

Taken together, these observations show that unlike the athermal deformation behavior observed in the μ-free pillars in Fig. 8, the deformation behavior of the μ-containing pillars in Fig. 9 exhibits a clear temperature-dependent deformation transition. At room temperature, the μ phases were retained as rigid structures, effectively impeding dislocation motion and serving as strong barriers against slip transmission. However, as an increase in temperature led to a gradual decline in the mechanical performance of the μ phase, allowing plastic bending or brittle shear fracture of the μ phase to occur. Consequently, the μ phases could no longer prevent dislocation glide, leading dislocations to propagate through the fragmented μ phases.

4. Discussion

4.1. Deformation behavior of the μ phase

In the current study, the μ phase exhibited a clear temperature-dependent transition in its mechanical behavior and in its role during deformation. At room temperature, the μ phase remained mechanically undeformed and acted as a strong barrier to slip transfer. Macro-scale compression followed by ECCI observation (Fig. 4) suggests that the μ phase remained undeformed, effectively blocking slip on $\{111\}_{\gamma/\gamma'}$ planes. Consistently, micropillar compression tests at room temperature (Fig. 9a) demonstrated that deformation occurred primarily along $\{111\}_{\gamma/\gamma'}$ slip planes parallel to the μ phases, confirming that the μ phases acted as rigid barriers without undergoing significant plastic deformation. This lack of plastic deformation in the μ phase at room temperature can be rationalized based on the geometric configuration illustrated in Fig. 2b. Specifically, the non-parallel $\{111\}_{\gamma/\gamma'}$ slip planes have an interplanar angle of approximately 70.6° with the basal plane of the μ phase, which is parallel to another $\{111\}_{\gamma/\gamma'}$ plane because of the orientation relationship. This geometric configuration makes basal slip—the slip plane with the lowest CRSS—highly unfavorable. In the case of the slip on the $\{111\}_{\gamma/\gamma'}$ planes parallel to the basal plane of the μ phase, the probability of direct dislocation transmission into the μ phase is extremely low. This is primarily because (i) the semi-coherent interface with significant lattice mismatch and associated strain fields prevents an exact crystallographic alignment between the active slip system in the γ/γ' matrix and a corresponding slip system in the μ phase, thereby inhibiting slip transmission; (ii) even when such an encounter does occur, the slip must traverse a large interfacial area to shear the μ-phase basal plane, and (iii) the Peierls barrier for dislocation motion inside the μ phase is significantly higher than that in the surrounding γ/γ' matrix [7]. For these geometric and energetic reasons, even if a dislocation approaches the μ phase along the basal-parallel plane, it is likely to be arrested within the μ phase or to deviate onto a secondary slip plane to bypass the precipitate, which requires additional thermal energy. Combined with the absence of thermal activation required for non-basal slip, dislocations therefore preferentially circumvent the μ phases rather than penetrating or deforming them.

In contrast, at elevated temperatures (≥ 500 °C), notable differences emerged. Macro-scale compression tests followed by ECCI observation (Fig. 5) clearly showed that slip no longer terminated at the μ phase but instead penetrated the precipitates together with bending and shearing of μ phases induced by slip at 700 °C. Additionally, *in situ* observation during micropillar compression tests over 500 °C (Fig. 9b) directly confirmed plastic deformation in a form of deformation-induced bending and shearing of the μ phases, indicating that the precipitate progressively lost its rigid barrier character as temperature increased. The detailed (S)TEM analyses (Fig. 6) further support this interpretation. In the specimen compressed at 700 °C, the μ phase showed deformation-induced bending and internal shear deformation with non-basal deformation modes. The observed slip traces suggest that deformation within the μ phase occurred predominantly along prismatic and pyramidal planes rather than by basal slip. Especially, the non-basal slips in the μ phase likely occurred on the 2nd order prismatic plane, i.e., $(11\bar{2}0)_\mu$, and 2nd order pyramidal planes, i.e., $(11\bar{2}4)_\mu$, $(11\bar{2}5)_\mu$, and $(11\bar{2}6)_\mu$, as schematically illustrated in Fig. 10a. Although direct identification of the atomic arrangement of each active slip plane would provide the most definitive crystallographic assignment, it was not feasible because of resolution limitations due to deformation. Therefore, the slip planes were inferred from the measured inclination angles of the slip traces with respect to the clearly identified basal plane of the μ phase. In addition, several regions showed that slip traces in the surrounding γ/γ' matrix were geometrically connected to deformation traces inside the μ phase, indicating that slip transmission across the μ phase can occur through specific crystallographic pathways, as illustrated in Fig. 10b. These observations collectively indicated a transition from slip blocking at room temperature to partial plastic accommodation and slip deformation of the μ phase at elevated temperature. Furthermore, the results consistently show that the μ phase is not simply brittle under all conditions. Instead, its response depends on temperature and on the geometric relationship between the active slip system of surrounding γ/γ' and the available deformation systems within the μ phase.

Regarding the mechanistic role and plasticity of the TCP phase, it has been considered that the TCP phase, such as the μ phase, has a generally detrimental effect on the mechanical properties of Ni-based superalloys due to (1) inherent brittle nature of the TCP phases, and (2) softening of the γ matrix caused by the depletion of refractory elements during TCP phase growth. However, recent studies have provided evidence contrary to the conventional perception of inherent brittleness, reporting that the μ phase does not necessarily fracture or exhibit interfacial decohesion during mechanical tests, and it can exhibit plasticity in some cases [24,32,36]. To better understand the precise influence of the μ phase on mechanical properties, several studies have recently focused on synthesizing bulk μ phases in binary or ternary alloy systems such as Fe_7Mo_6 [26,37], Co_7Nb_6 [29], Nb_7Ni_6 [30], Ta_7Fe_6 [30], and Ta-Fe(−Al) [31], and subsequently investigating their deformation mechanisms using micro-mechanical testing methods. These studies revealed that the most common deformation mechanism for bulk μ phase involves slip on the basal plane $(0001)_\mu$, typically via conventional hexagonal slip or synchro-shear [26], due to their inherently lower CRSS [30]. While basal slip readily occurs even at room temperature, non-basal slips, such as prismatic and pyramidal slips, have been reported primarily at elevated temperatures [28,29]. The activation of these non-basal slips requires both dislocation glide and thermally-assisted atomic transport to maintain the local TCP packing rules intrinsic to their Frank-Kasper polyhedral crystal structure [30], making them relatively unfavorable compared to basal slip. Among non-basal slip systems, deformation typically occurs via 1st order prismatic plane, i.e., $(1\bar{1}00)_\mu$, and 1st order pyramidal planes, i.e., $(1\bar{1}01)_\mu$, $(1\bar{1}02)_\mu$, $(1\bar{1}05)_\mu$ [30], and $(1\bar{1}0\ 26)_\mu$ [31], depending on local atomic coordination environments.

The present results are broadly consistent with earlier studies on micromechanical experiments of bulk μ phases, which showed that the μ

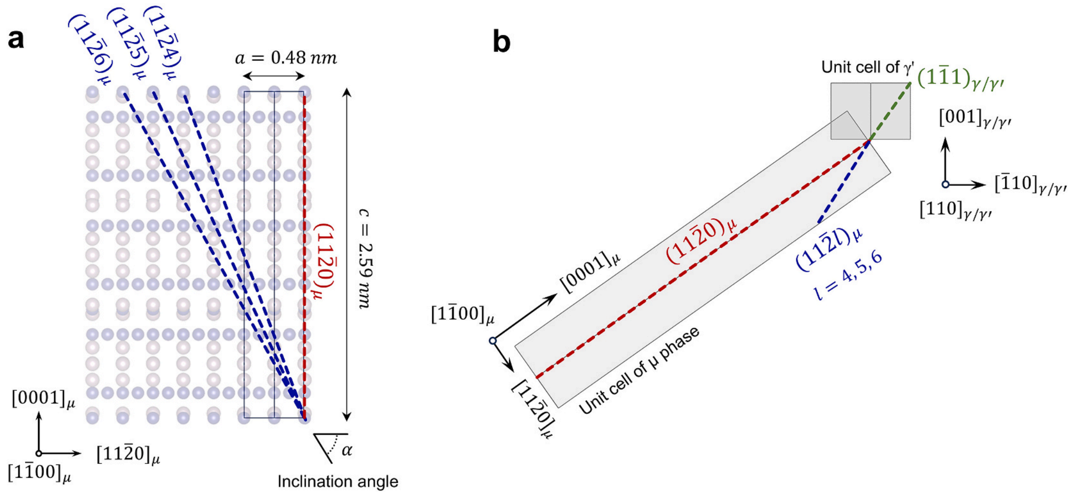

Fig. 10. (a) An atomic structure illustration of the μ phase viewed along $[1\bar{1}00]_\mu$, highlighting potential slip planes activated during deformation. The red-colored plane corresponds to prismatic $(11\bar{2}0)_\mu$ plane and the blue-colored planes indicate pyramidal $(11\bar{2}l)_\mu$ ($l = 4, 5, 6$) planes, inclined at varying angles (denoted as inclination angle α) with respect to the basal plane, which are 61, 65, and 69° for $(11\bar{2}4)_\mu$, $(11\bar{2}5)_\mu$, and $(11\bar{2}6)_\mu$, respectively. (b) A schematic diagram demonstrating the crystallographic orientation relationship between the potential slip planes in the μ phase and the $(1\bar{1}1)_{\gamma/\gamma'}$ octahedral slip plane of the adjacent γ/γ'. The geometrical relationship indicates possible slip transfer mechanism from octahedral slip plane (green line) of the γ/γ' to prismatic (red line) and pyramidal (blue line) slip planes of the μ phase. (For interpretation of the references to colour in this figure legend, the reader is referred to the web version of this article.)

phase can exhibit plasticity rather than purely brittle failure and the non-basal slip systems become more active at elevated temperatures. However, the deformation mechanisms identified in this study deviate from previous findings for bulk μ phases in two notable ways. First, basal slip did not appear to dominate the deformation response in the present study, despite its intrinsically lower critical resolved shear stress reported in bulk studies. Second, the experimentally observed deformation paths are more consistent with 2nd order prismatic and pyramidal planes than with the 1st order non-basal planes commonly discussed for bulk μ phases [26,29–31]. These differences indicate that the deformation behavior of μ phases precipitated inside a γ/γ' matrix cannot be understood solely from the intrinsic slip behavior of bulk μ phases. Instead, it must also be interpreted in terms of the crystallographic constraints imposed by the surrounding γ/γ' microstructure. Owing to the experimentally observed orientation relationship, the basal plane of the μ phase is laterally aligned with one of the $\{111\}_{\gamma/\gamma'}$ of the surrounding γ/γ', while the other active $\{111\}_{\gamma/\gamma'}$ slip planes intersect the μ phase at a high angle. Under this geometric condition, direct activation of basal slip does not necessarily provide the most favorable route for slip. Rather, deformation transfer appears to depend on whether the incident matrix slip can be accommodated by crystallographically compatible non-basal planes within the μ phase. As shown schematically in Fig. 10b, slips on 2nd order prismatic and pyramidal planes align favorably with slip directions in the γ/γ' through only a tilt mechanism at their mutual edges. In contrast, slip along 1st order prismatic and pyramidal planes, as previously reported in bulk phases, would require simultaneous tilt and a 30° twist to accommodate slip continuity, creating a significantly higher energy barrier for deformation propagation [38]. This geometrical constraint also explains why the μ phase acts as a rigid barrier at room temperature, where thermally assisted non-basal deformation is limited, but becomes more deformable at elevated temperatures, where additional slip accommodation through prismatic and pyramidal systems becomes possible.

Based on the above observations and analyses, the proposed deformation mechanisms and possible deformation pathways for plate-like μ phases precipitated within single crystal Ni-based superalloys are schematically summarized in Fig. 11. As illustrated in Fig. 11a, the plate-like μ phase initially precipitates with its $(0001)_\mu$ basal plane laterally aligned parallel to the $\{111\}_{\gamma/\gamma'}$ plane, maintaining an interplanar angle of approximately 70.6° with respect to non-parallel $\{111\}_{\gamma/\gamma'}$ plane. During high-temperature deformation, slip propagating along the $\{111\}_{\gamma/\gamma'}$ plane induces deformation within the μ phase, facilitating slip transmission through specific crystallographic paths, as shown in Fig. 11b and c. Two main deformation scenarios are identified: paths without bending deformation (paths A1 and A2) and paths with bending deformation (paths B1 and B2). For deformation paths without bending (A1 and A2), slip directly penetrates the μ phase via 2nd order prismatic $(11\overline{2}0)_\mu$ or pyramidal planes $(11\overline{2}l)_\mu$ $(l = 4,\ 5,\ 6)$. Under these conditions, the theoretical tilt angles required for slip continuity are estimated to be 19.4° for the prismatic plane and ranging from 0.9 to 9.7° for pyramidal planes. Otherwise, for deformation paths involving μ phase bending (B1 and B2), slip proceeds through 2nd order prismatic or pyramidal planes after the μ phase has undergone bending deformation. Experimental observations from ECCI (Fig. 5) and (S)TEM (Fig. 6) indicated that the bending angles range between approximately 8–15°. Assuming that the bending angle is 10°, the theoretical tilt angles are estimated to be around 9.4° for prismatic plane and ranging from 10.9 to 19.7° for pyramidal planes.

Assuming that the barrier for slip propagation scales with the required tilt angle, pyramidal slip would be favorable deformation mode in the absence of bending, whereas prismatic slip becomes more advantageous after bending has occurred. However, due to the extensive deformation observed in this study, precise atomic-scale deformation configurations and quantitative stress requirements for each slip system could not be definitively characterized *postmortem*. Therefore, detailed follow-up investigations that precisely measure the required stress and analyze atomic-scale configurations for each potential deformation pathway are essential to conclusively identify the most energetically favorable slip mechanisms within μ phases under realistic deformation conditions.

It should be noted that under prolonged high-temperature exposure in practical alloys, TCP phases may evolve into interconnected network morphologies accompanied by substantial coarsening and irregularization of the surrounding γ/γ' microstructure. In such cases, the well-defined cuboidal γ/γ' microstructure present in the current study may no longer exist, and deformation is expected to depend more strongly on

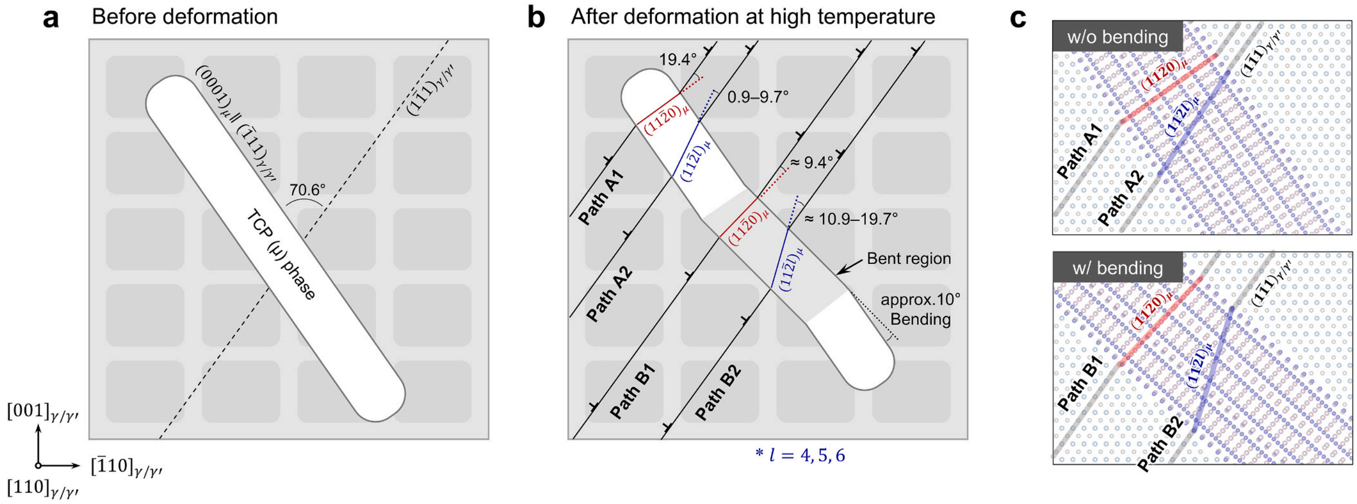

Fig. 11. Schematic illustration depicting possible deformation paths associated with slip intersections between the μ phase and the surrounding γ/γ', viewed along the $[110]_{\gamma/\gamma'}$. (a) Initial crystallographic relationship prior to deformation, showing the basal plane of the μ phase inclined at 70.6° to the $(1\overline{1}1)_{\gamma/\gamma'}$ slip plane. (b) Potential slip paths and their tilt angles during deformation at high temperature and (c) corresponding atomic-scale schematic comparison of the slip paths accompanying tilt mechanism without and with bending of the μ phase: paths A1 and A2 represent slip transfer through the μ phase via prismatic $(11\overline{2}0)_\mu$ plane (red line) and pyramidal $(11\overline{2}l)_\mu$ $(l = 4,\ 5,\ 6)$ planes (blue line), respectively. Paths B1 and B2 represent similar transfer possibilities after bending deformation (about 10°) of the μ phase. Corresponding inclination angles between the slip planes in the γ/γ' and the μ phases are provided to demonstrate the feasibility of these deformation pathways. (For interpretation of the references to colour in this figure legend, the reader is referred to the web version of this article.)

the mechanical response of the coarse and irregular γ′ phases and on stress redistribution among multiple TCP precipitates. Consequently, the slip-transfer mechanisms identified here for isolated μ plates may not fully represent the deformation behavior of interconnected TCP networks formed during long-term exposure.

4.2. Role of the μ phase in the strength at various temperatures

The CRSS values obtained from macro- and micro-scale compression tests over a wide temperature range are summarized in Fig. 12a. At the macro-scale, the exposed specimens containing a higher density of μ phase consistently exhibited CRSS values approximately 100 MPa lower than the unexposed specimens across all investigated temperatures. A comparable reduction in CRSS was also observed at the micro-scale: μ-containing micropillars extracted from the exposed samples showed a similarly reduced CRSS, by about 100 MPa, compared to μ-free micropillars from the unexposed samples, irrespective of the testing temperature. The observation that a nearly identical magnitude of CRSS reduction is present at both length scales suggests that the dominant softening mechanism is not governed by size-dependent effects.

Although precipitates are generally expected to strengthen the material—particularly in small-volume tests such as micropillar compression—this expectation is not met in the present case. Instead, the observed reduction in yield stress can be rationalized by the dominant contribution of microstructural softening in the γ/γ′ matrix surrounding the μ phase, which outweighs the intrinsic hardening effect of the precipitates. The microstructural and compositional characterization of the μ phase was previously reported in detail in [32] for the same specimen batch, where the room temperature mechanical response was examined. The present study builds directly on that work and focuses on deformation behavior at different temperatures. As reported in [32] for the same materials, the formation of the μ phase during the additional 1000 °C exposure leads to a reduction in the γ' volume fraction from 69 to 65%, which was attributed to the low equilibrium volume fraction of γ' phase (54.6%) supported by thermodynamic calculations for the present alloy. It suggests that partial dissolution of γ' occurs during high-temperature exposure, thereby reducing the strengthening contribution of the γ' phase. In addition, the reduced γ' volume fraction results in an increase in the average γ channel width from approximately 40 to 47 nm, further decreasing the resistance to dislocation motion and contributing to the observed strength reduction. Furthermore, APT analysis performed in [32] revealed measurable compositional depletion of μ-forming elements in the γ matrix due to μ formation. Specifically, the concentrations of Co, Cr, and W in the γ matrix decreased by approximately 3.0, 3.7, and 1.9 at.%, respectively. When multiplied by their corresponding solid-solution strengthening coefficients, this compositional redistribution results in a calculated reduction in γ matrix strengthening from 335 to 312 MPa. The combined reduction in γ' volume fraction and γ matrix solid solution strengthening provides quantitative support for the observed decrease in CRSS. The present results demonstrate that this γ/γ' softening effect remains decisive over the entire investigated temperature range up to 700 °C.

One notable observation is the contrasting temperature dependence of CRSS between macro- and micro-scale compression tests with increasing temperature (Fig. 12b). While the macro-scale tests exhibit a slight reduction in strength of approximately 30 MPa (−6% decrease)

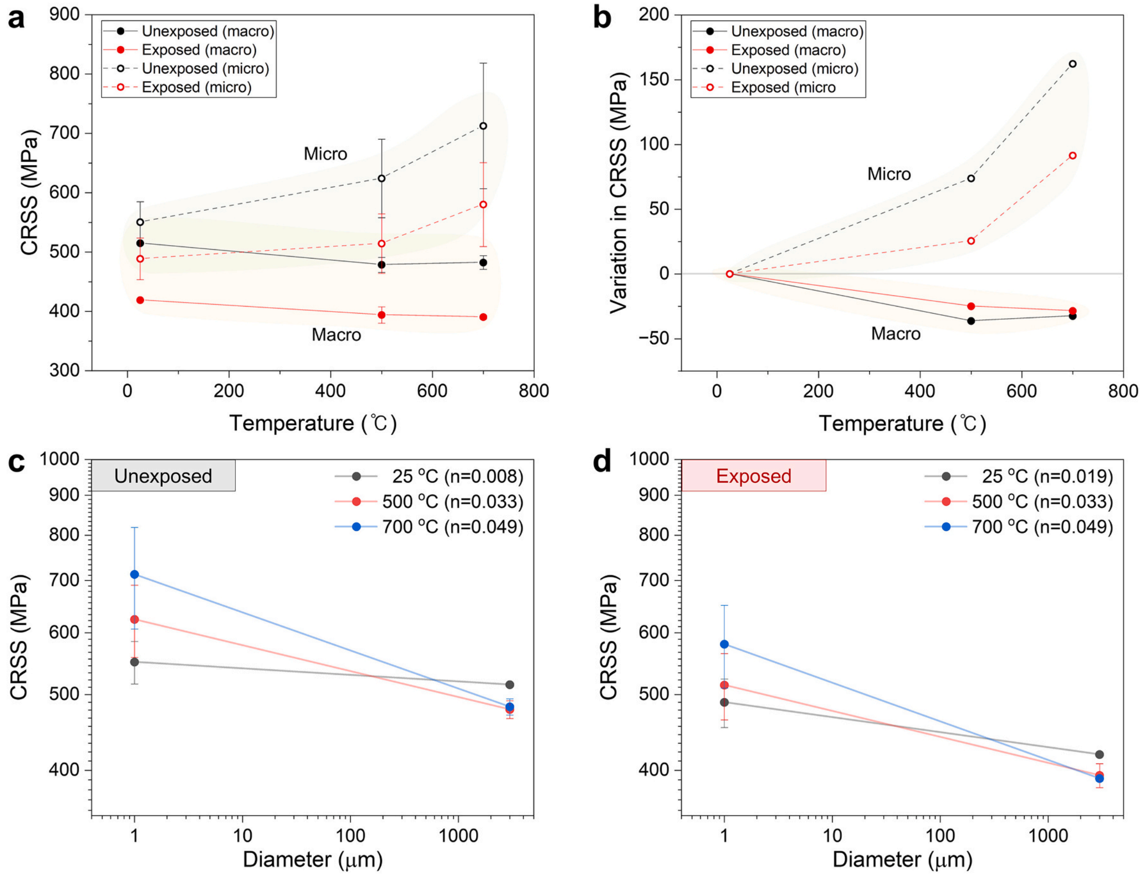

Fig. 12. Temperature-dependent trends in CRSS obtained from macro- and micro-scale compression tests. (a) Comparison of absolute CRSS values for unexposed (black-colored) and exposed (red-colored) samples at different temperatures, measured via macro-scale (solid symbol) and micro-scale (open symbols) compression testing. (b) Relative change in CRSS at elevated temperatures compared to room temperature ($CRSS_{High\ Temp.} - CRSS_{Room\ Temp.}$), highlighting the degree of temperature-induced variation in mechanical properties. The temperature-dependent of size effect of (c) the unexposed and (d) the exposed samples obtained from macro- and micro-scale compression tests. (For interpretation of the references to colour in this figure legend, the reader is referred to the web version of this article.)

relative to room temperature, the micro-scale tests show a systematic increase in CRSS with temperature (increase of + 29% for the unexposed and + 19% for the exposed samples). This opposite trend indicates that different deformation-controlling mechanisms become active at the microscale at elevated temperatures triggering yield-stress anomaly at lower temperature. The observed strengthening in the micro-scale tests suggests that thermally activated mechanisms may raise the yield stress at the microscale. Nevertheless, these effects are not pronounced at the macroscale.

As represented in Fig. 12c and d, an apparent size dependence of the CRSS is observed for both the unexposed and exposed samples at different temperatures. Although this comparison is based on a limited dataset consisting of only two diameters, a consistent trend can be observed. The size effect was evaluated using the power-law relationship,

$$\sigma = AD^{-n} \tag{2}$$

where σ is the CRSS, A is a constant, D is the specimen diameter, and n is the size-effect exponent. At room temperature, the measured exponent values were 0.008 for the unexposed sample and 0.019 for the exposed sample, indicating a measurable difference between the two conditions but remaining significantly lower than the typical exponent values reported for FCC metals ($n \approx 0.61$–0.97) [39]. This could be attributed to the intrinsic microstructural length scales, associated with the fine γ/γ' microstructure, limiting the magnitude of classical size effects in the present alloy.

With increasing temperature, the exponent increases and converges to similar values for both conditions, reaching 0.033 at 500 °C and 0.049 at 700 °C. Despite the considerable difference in CRSS between the unexposed and exposed samples, the comparable power-law exponents obtained at elevated temperature suggest that the temperature-dependent strengthening observed in the micropillar tests is likely influenced by size-dependent effects associated with the high surface-to-volume ratio of the pillars. The enhancement of size effects with increasing temperature has been reported in several previous studies. For example, Soler et al. [40] demonstrated for LiF single crystals that the flow stress can be decomposed into the lattice resistance, forest hardening, and size-dependent stresses. As temperature increases, the contributions from lattice resistance and forest hardening decrease, making the size-dependent contribution relatively more dominant. Similarly, Torrents Abad et al. [41] observed an increase in the size-effect exponent with increasing temperature in Ta and W micropillars, which was attributed to reduced lattice friction and the resulting increased importance of size-controlled plasticity.

Based on these observations, the strengthening observed at the micro-scale in the present study can be partially attributed to the enhanced contribution of size-dependent mechanisms at elevated temperatures. As size-independent strengthening contributions diminish, plastic deformation becomes increasingly sensitive to external dimensions and boundary conditions, promoting source-limited plasticity. In addition, dislocation annihilation may be facilitated at elevated temperatures, which can lead to dislocation starvation and corresponding increase in the flow stress. The large surface-to-volume ratio of micropillars may also enhance surface image forces, facilitating cross-slip processes [42]. In Ni-based superalloys, cross-slip of superdislocations in the γ' phase may promote Kear–Wilsdorf locking [43], which can further contribute to strengthening at elevated temperatures.

It should be noted, however, that in Ni-based superalloys the characteristic microstructural length scale is typically small due to the fine γ/γ' microstructure, which may suppress classical mechanical size effects, particularly at lower temperatures. In this regime, plastic deformation is primarily governed by intrinsic microstructural constraints rather than external specimen dimensions. At elevated temperatures, however, deformation of the γ' phase becomes increasingly active, effectively increasing the operative characteristic length scale. As a result, the relative influence of specimen size can become more pronounced, leading to an enhanced size effect. This provides a plausible explanation for the contrasting temperature dependence of CRSS observed between macro- and micro-scale tests.

Nevertheless, it should be emphasized that the present interpretation is based on a limited dataset and therefore remains preliminary. A more comprehensive assessment would require systematic compression tests over a wider range of specimen diameters, combined with detailed characterization of the underlying deformation mechanisms across different length scales.

5. Conclusion

In the present study, macro- and micro-scale compression experiments were systematically performed to investigate the role of μ-type TCP phases on the mechanical behavior of Ni-based single-crystal superalloys across a wide temperature range from 25 up to 700 °C. Through detailed defect analyses, using ECCI and STEM observations, and strength evaluations conducted in multi-scale, the following key findings were obtained:

- At room temperature, the plate-like μ phase remained undeformed and acted as a strong barrier to the propagation of $\{111\}_{\gamma/\gamma'}$ slip. However, at elevated temperatures (≥ 500 °C), thermally-assisted atomic transport facilitated deformation within the μ phase. Consequently, the μ phase underwent bending and exhibited plasticity through shearing along non-basal crystallographic planes.
- Activated non-basal slip planes within the μ phase were identified as 2nd order prismatic $(11\overline{2}0)_{\mu}$ plane and 2nd order pyramidal $(11\overline{2}4)_{\mu}$, $(11\overline{2}5)_{\mu}$, and $(11\overline{2}6)_{\mu}$ planes. The specific potential deformation paths were suggested based on the inclination angle relative to the $\{111\}_{\gamma/\gamma'}$ slip planes and the occurrence of bending deformation.
- Both macro- and micro-scale compression tests revealed consistently lower CRSS values in μ-containing specimens across all temperatures. These trends suggest that the reduced strength in μ-containing samples primarily arises from microstructural softening in the γ/γ' matrix rather than the μ phase itself.
- However, opposite temperature dependencies were observed between macro- and micro-scale: a slight softening at the macroscale and a strengthening at the microscale. It might be attributed to surface- and diffusion-related sample size effects may additionally contribute to the strengthening behavior observed in micropillars.

In summary, these findings provide a comprehensive understanding of the temperature-dependent deformation behavior of the μ phase and its effects on the mechanical performance of Ni-based single-crystal superalloys. Future research should further focus on atomic configuration and required stress for individual slip systems within μ phases, thereby enabling more precise predictions of alloy performance under practical operating conditions.

CRediT authorship contribution statement

Sangwon Lee: Writing – original draft, Visualization, Methodology, Investigation, Data curation, Conceptualization. **Jeonghyeon Do:** Writing – review & editing, Methodology, Investigation. **Baig Gyu Choi:** Writing – review & editing, Funding acquisition. **Joong Eun Jung:** Writing – review & editing. **In Soo Kim:** Writing – review & editing. **Ujjval Bansal:** Writing – review & editing, Investigation, Data curation. **Christoph Kirchlechner:** Writing – review & editing, Project administration, Funding acquisition, Conceptualization. **Pyuck-Pa Choi:** Writing – review & editing, Supervision, Funding acquisition, Conceptualization. **Subin Lee:** Writing – review & editing, Supervision, Project administration, Funding acquisition, Conceptualization.

Declaration of competing interest

The authors declare that they have no known competing financial interests or personal relationships that could have appeared to influence the work reported in this paper.

Acknowledgment

This work was supported by the Materials Platform Technology Development Project (PNK8890, Development of Single Crystal Superalloy for Gas Turbine) funded by the Ministry of Science and ICT (MSIT, South Korea), and by the framework of international cooperation program through the National Research Foundation of Korea (NRF), funded by Ministr (NRF-2022K2A9A2A15000110). S. Lee acknowledges financial support from the DAAD–NRF GEnKO Program. C. Kirchlechner acknowledges financial support from the Deutsche Forschungsgemeinschaft (DFG) within Project No. 500076185 “Micromechanical characterization of grain boundary slip: Towards a deformation mechanism map”. Transmission electron microscopy (TEM) investigations were carried out with the support of the Karlsruhe Nano Micro Facility (KNMFi), a Helmholtz Research Infrastructure at the Karlsruhe Institute of Technology.

Appendix A. Supplementary data

Supplementary data to this article can be found online at https://doi.org/10.1016/j.matdes.2026.116141.

Data availability

Data will be made available on request.

References

[1] R.C. Reed. The Superalloys: Fundamentals and Applications, Cambridge University Press, 2006.

[2] E. Ito, I. Okada, K. Tsukagoshi, J. Masada, Development of Key Technologies for the Next Generation High Temperature Gas Turbine, in: Vol. 3 Control. Diagnostics Instrumentation; Educ. Electr. Power; Microturbines Small Turbomachinery; Sol. Brayt. Rank. Cycle, ASMEDC, 2011: pp. 579–586.

[3] M. Ishikawa, T. Komori, M. Terauchi, J. Yasuraoka, Development of high efficiency gas turbine combined cycle, Tech. Rev. Mitsubishi Heavy Ind. 45 (2008) 15–17.

[4] T. Saito, H. Harada, T. Yokokawa, M. Osawa, K. Kawagishi, S. Suzuki, Raft structure of nickel base single-crystal superalloys, Mater. Trans. 65 (2024) MT-M2024081.

[5] G. Gudivada, A.K. Pandey, Recent developments in nickel-based superalloys for gas turbine applications: review, J. Alloys Compd. 963 (2023) 171128.

[6] J. Zhang, F. Lu, T. Huang, R. Li, G. Zhang, L. Liu, An advanced approach to improve the high-temperature property for Ni-based superalloys: interface segregation manipulation, Mater. Sci. Eng. A 881 (2023) 145382.

[7] H. ur Rehman, K. Durst, S. Neumeier, A.B. Parsa, A. Kostka, G. Eggeler, M. Göken, Nanoindentation studies of the mechanical properties of the μ phase in a creep deformed Re containing nickel-based superalloy, Mater. Sci. Eng. A 634 (2015) 202–208.

[8] K. Matuszewski, A. Müller, N. Ritter, R. Rettig, K.J. Kurzydłowski, R.F. Singer, On the thermodynamics and kinetics of TCP phase precipitation in Re- and Ru-containing Ni-base superalloys, Adv. Eng. Mater. 17 (2015) 1127–1133.

[9] Y. Cheng, X. Zhao, W. Xia, Q. Yue, Y. Gu, Z. Zhang, The overview of the formation mechanisms of topologically close-packed phases in Ni-based single crystal superalloys, Mater. Des. 237 (2024) 112582.

[10] Y. Zhao, X. Zhao, X. Qi, Y. Cheng, J. Zou, Y. Wang, X. Qu, Q. Yu, Z. Zhang, The origin of the straight propagation of the σ phase in a Ni-based single crystal superalloy at elevated temperature, Acta Mater. 275 (2024).

[11] A. Mottura, R.C. Reed, What is the role of rhenium in single crystal superalloys? MATEC Web Conf. 14 (2014) 01001.

[12] Y. Han, W. Ma, Z. Dong, S. Li, S. Gong, Effect of Ruthenium on Microstructure and Stress Rupture Properties of a Single Crystal Nickel-Base Superalloy, in: Superalloys 2008 (Eleventh Int. Symp., TMS, 2008: pp. 91–97.

[13] S. Lee, J. Do, K. Jang, H. Jun, Y. Park, P. Choi, Promotion of topologically close-packed phases in a Ru-containing Ni-based superalloy, Scr. Mater. 222 (2023) 115041.

[14] J.Y. Chen, Q. Feng, Z.Q. Sun, Topologically close-packed phase promotion in a Ru-containing single crystal superalloy, Scr. Mater. 63 (2010) 795–798.

[15] X. Lv, J. Zhang, Q. Feng, The promotion of Ru on topologically close-packed phase precipitation in the high Cr-containing (∼9wt.%) nickel-base single crystal superalloy, J. Alloys Compd. 648 (2015) 853–857.

[16] J. Sun, J. Liu, J. Li, C. Chen, X. Wang, Y. Zhou, X. Sun, Dual effects of Ru on the microstructural stability of a single crystal superalloy, Scr. Mater. 205 (2021) 114209.

[17] M. Pessah-Simonetti, P. Caron, T. Khan, Effect of a long-term prior aging on the tensile behaviour of a high-performance single crystal superalloy, Le, J. Phys. IV 03 (1993) C7–347-C7-350.

[18] A. Volek, R.F. Singer, R. Buergel, J. Grossmann, Y. Wang, Influence of topologically closed packed phase formation on creep rupture life of directionally solidified nickel-base superalloys, Metall. Mater. Trans. A Phys. Metall. Mater. Sci. 37 (2006) 405–410.

[19] Q. Shi, X. Ding, J. Chen, X. Zhang, Y. Zheng, Q. Feng, Fracture mode of a Ni-based single crystal superalloy containing topologically close-packed phases at ambient temperature, Metall. Mater. Trans. A 45 (2014) 1665–1669.

[20] W. Guo, H. Zhao, Y. Ru, Y. Pei, J. Wang, Q. Liu, X. Li, H. Wang, S. Zhang, S. Gong, S. Li, Topologically closed packed phase and its interaction with dislocation movement in Ni–based superalloy during high–temperature creep, Crystals 12 (2022).

[21] A.C. Yeh, S. Tin, Effects of Ru on the high-temperature phase stability of Ni-base single-crystal superalloys, Metall. Mater. Trans. A Phys. Metall. Mater. Sci. 37 (2006) 2621–2631.

[22] P. Zhao, G. Xie, C. Chen, X. Wang, P. Zeng, F. Wang, J. Zhang, K. Du, Interplay of chemistry and deformation-induced defects on facilitating topologically-close-packed phase precipitation in nickel-base superalloys, Acta Mater. 236 (2022) 118109.

[23] Z. Wang, Y. Li, H. Zhao, L. Chen, Z. Zhang, D. Shen, M. Wang, Evolution of μ phase in a Ni-based alloy during long-term creep, J. Alloys Compd. 782 (2019) 1–5.

[24] M. Simonetti, P. Caron, Role and behaviour of μ phase during deformation of a nickel-based single crystal superalloy, Mater. Sci. Eng. A 254 (1998) 1–12.

[25] Z. Xie, D. Chauraud, A. Atila, E. Bitzek, S. Korte-Kerzel, J. Guénolé, Unveiling the mechanisms of motion of synchro-Shockley dislocations in Laves phases, Phys. Rev. Mater. 7 (2023) 1–12.

[26] S. Schröders, S. Sandlöbes, C. Birke, M. Loeck, L. Peters, C. Tromas, S. Korte-Kerzel, Room temperature deformation in the Fe7Mo6 μ-phase, Int. J. Plast 108 (2018) 125–143.

[27] Y. Zhang, K. Du, W. Zhang, B. Du, D. Qi, W. Li, M. Song, L. Sheng, H. Ye, Shear deformation determined by short-range configuration of atoms in topologically close-packed crystal, Acta Mater. 179 (2019) 396–405.

[28] Y. Cheng, G. Wang, J. Liu, L. He, Atomic configurations of planar defects in μ phase in Ni-based superalloys, Scr. Mater. 193 (2021) 27–32.

[29] W. Luo, Z. Xie, P.-L. Sun, J.-S.-K.-L. Gibson, S. Korte-Kerzel, Plasticity of the Nb-rich μ-Co7Nb6 phase at room temperature and 600°C, Acta Mater. 246 (2023) 118720.

[30] W. Luo, C. Gasper, S. Zhang, P.L. Sun, N. Ulumuddin, A. Petrova, Y. Lysogorskiy, R. Drautz, Z. Xie, S. Korte-Kerzel, Non-basal plasticity in the μ-phase at room temperature, Acta Mater. 277 (2024) 120202.

[31] C. Gasper, E.M. Soysal, N. Ulumuddin, T. Stollenwerk, T. Reclik, P.L. Sun, S. Korte-Kerzel, Mechanical properties and deformation mechanisms of the C14 Laves and μ-phase in the ternary Ta-Fe(-Al) system, Mater. Des. 251 (2025) 113625.

[32] S. Lee, J. Do, B.G. Choi, U. Bansal, C. Kirchlechner, P.P. Choi, S. Lee, Local plastic deformation in the vicinity of topologically close-packed phases in a Ni-based single crystal superalloy, Mater. Des. 250 (2025) 113600.

[33] D.A. Porter, K.E. Easterling, K.E. Easterling, Phase Transformations in Metals and Alloys, CRC Press, 2009.

[34] X.Z. Qin, J.T. Guo, C. Yuan, G.X. Yang, L.Z. Zhou, H.Q. Ye, μ-Phase behavior in a cast Ni-base superalloy, J. Mater. Sci. 44 (2009) 4840–4847.

[35] G. Dehm, B.N. Jaya, R. Raghavan, C. Kirchlechner, Overview on micro- and nanomechanical testing : new insights in interface plasticity and fracture at small length scales, Acta Mater. 142 (2018) 248–282.

[36] J.X. Yang, Q. Zheng, X.F. Sun, H.R. Guan, Z.Q. Hu, Formation of μ phase during thermal exposure and its effect on the properties of K465 superalloy, Scr. Mater. 55 (2006) 331–334.

[37] S. Schröders, S. Sandlöbes, B. Berkels, S. Korte-Kerzel, On the structure of defects in the Fe7Mo6 μ-phase, Acta Mater. 167 (2019) 257–266.

[38] X. Zhang, F.P.E. Dunne, 3D CP-XFEM modelling of short crack propagation interacting with twist/tilt nickel grain boundaries, J. Mech. Phys. Solids 168 (2022) 105028.

[39] M.D. Uchic, P.A. Shade, D.M. Dimiduk, Plasticity of micrometer-scale single crystals in compression, Annu. Rev. Mater. Res. 39 (2009) 361–386.

[40] R. Soler, J.M. Wheeler, H.J. Chang, J. Segurado, J. Michler, J. Llorca, J.M. Molina-Aldareguia, Understanding size effects on the strength of single crystals through high-temperature micropillar compression, Acta Mater. 81 (2014) 50–57.

[41] O. Torrents Abad, J.M. Wheeler, J. Michler, A.S. Schneider, E. Arzt, Temperature-dependent size effects on the strength of Ta and W micropillars, Acta Mater. 103 (2016) 483–494.

[42] Y. Cui, G. Po, N. Ghoniem, Temperature insensitivity of the flow stress in body-centered cubic micropillar crystals, Acta Mater. 108 (2016) 128–137.

[43] R.C. Reed, C.M.F. Rae, Physical Metallurgy of the Nickel-based Superalloys, Elsevier, Fifth Edit, 2014.